



Testing the effects of aspect and total insolation on luminescence depth profiles for rock surface exposure dating

S. Fuhrmann^{a,*}, M.C. Meyer^a, L.A. Gliganic^{a,b}, F. Obleitner^c

^a Department of Geology, University Innsbruck, Austria

^b Centre for Archaeological Sciences, University of Wollongong, Australia

^c Department of Atmospheric and Cryospheric Sciences, University Innsbruck, Austria

ARTICLE INFO

Keywords:

Rock surface dating
Luminescence dating
OSL
Calibration
Optically stimulated luminescence

ABSTRACT

Using luminescence to date the burial and exposure ages of rock surfaces has been a revolutionary new geochronological approach developed and refined over the past decade. Rock surface exposure dating is based on the principle that the depth to which the luminescence signal is bleached into a rock surface is dependent on the duration of that rock surface's exposure to sunlight. However, given the recentness of method development, the effects of basic light exposure variables such as the orientation of rock surfaces and the incidence angle of incoming light on bleaching depth have not been tested. We designed an experiment in which we controlled the exposure duration (t) and orientation of granite and sandstone samples while measuring the light attenuation coefficient (μ) and the photon flux at the rock surface (φ_0) to determine the influence of spatial orientation of a rock surface on its respective bleaching depth. Our results confirm that the opacity of the rock (μ) and the total insolation have significant effects on the bleaching depth for vertically oriented surfaces. We also observed that the bleaching depth is strongly related to the incidence angle at which the sunlight hits the rock surface, indicating that the effectiveness of bleaching of a given rock surface follows seasonal cycles. Our data suggest that optimal calibration samples for rock surface exposure dating should be of the same lithology and have the same geographical location and orientation of the target sample. Additionally, calibration samples should be collected in year increments so that no season's solar incidence angles are preferred.

1. Introduction

Over the last decades, optically stimulated luminescence (OSL) dating has evolved into a well-established numerical dating technique in the Quaternary Sciences that has seen a number of methodological inventions. Classical OSL dating allows determining the burial age of sand- and silt-sized sediments from estimates of absorbed doses and dose rate (Huntley et al., 1985; Rhodes, 2011). Recently, this approach has been adapted to also determine the burial age of geological and archaeological rock surfaces (e.g. Chapot et al., 2012; Gliganic et al., 2021; Greilich et al., 2005; Jenkins et al., 2018; Liritzis, 2011; Liu et al., 2019; Simkins et al., 2013; Simms et al., 2011; Sohbaty et al., 2012). This latter variant of optical dating is referred to as OSL rock surface burial dating (RSBD) and is based on the circumstance that all traps inside the crystalline structure of a rock are filled with electrons, giving rise to a saturated OSL signal upon optical stimulation. Daylight exposure causes these electron traps to be gradually emptied in the topmost millimetres to centimetres

of a fresh rock surface and the OSL signal to be reset (or bleached). Upon burial, a natural dose re-accumulates in the previously bleached rock surface, due to naturally occurring ionizing radiation from the rock itself and the surrounding sediment that shields the rock surface from further daylight exposure. Hence, similar to sediment burial dating, estimates of dose rate and (re-)accumulated dose in a given rock surface allow the time since burial to be constrained.

The fact that light penetrates into rock surfaces, albeit on a mm to cm scale only, and thus gradually bleaches the OSL signals, can also be exploited to determine the time elapsed since a rock surface has been subjected to daylight exposure. This approach is referred to as OSL rock surface exposure dating (RSeD) and has been used to determine the age of e.g. rock paintings (Chapot et al., 2012), negative flake scars (Gliganic et al., 2021), or the emplacement of coastal tsunami boulders (Brill et al., 2012) and other rock surfaces (Polikreti, 2007; Polikreti et al., 2003; Sohbaty et al., 2012).

The methodological foundation for RSeD has been laid by Polikreti

* Corresponding author.

E-mail address: stephan.fuhrmann@uibk.ac.at (S. Fuhrmann).

et al. (2003) and picked up and developed further by [Sohbati et al. \(2011\)](#) and [Laskaris and Liritzis \(2011\)](#). Because daylight exposure is gradually resetting the OSL signal in the topmost section of a fresh rock surface a characteristic OSL-depth profile evolves over time, with no OSL signal remaining at the very surface and a gradual (S-shaped) OSL signal build-up with depth below the rock surface. RSeD exploits the circumstance that the depth as well as the shape of the OSL bleaching front is closely related to the time that has elapsed since the fresh rock surface has first been exposed to light ([Meyer et al., 2018](#); [Sohbati et al., 2012](#)). Hence, deriving an exposure age from the depth and shape of an OSL profile requires an accurate bleaching-with-depth model to be fitted to the OSL data and the relevant model parameters to be constrained. The currently most widely used model for RSeD is that of [Sohbati et al. \(2012a,b\)](#), which is a double exponential function based on first order luminescence kinetics from a single luminescence trap (Equation (1)):

$$L = L_0 e^{-\frac{\sigma \varphi_0 t}{\mu}} e^{-\mu x} \quad (1)$$

In this model, L represents the luminescence signal at a given depth x [mm] and L_0 is the maximum luminescence signal intensity prior to exposure to sunlight (i.e. the unbleached, saturated luminescence level from the light protected interior of the rock). σ [cm²] is the photoionization cross section and φ_0 [cm⁻² s⁻¹] the incident solar photon flux at the rock surface. Thus $\frac{\sigma \varphi_0}{\mu}$ represents the effective detrapping rate of the luminescence signal at the surface, while μ [mm⁻¹] is the rock-specific light attenuation coefficient and t delineates the exposure duration. Both, μ and σ are rock and mineral specific parameters and thus directly dependent on the sample lithology.

In order to calculate the correct exposure duration (t), RSeD requires calibration of the model parameters μ and $\frac{\sigma \varphi_0}{\mu}$. Typically, this involves the measurement of a known-age calibration sample ([Sohbati et al., 2012a,b](#); [Gliganic et al., 2019](#)). It has been suggested that the rock surface used for calibrating the model parameters should be of the same lithology as the rock surface targeted for dating and have a known exposure history ([Sohbati et al., 2012](#)). Sometimes an independent rock surface of known age is available at the sampling site for this calibration (e.g., [Sohbati et al., 2012a,b](#)). Alternatively, a fresh calibration surface in close spatial proximity to the sampling site can be artificially created for that purpose (e.g. [Gliganic et al., 2019](#)). After some time to allow a new OSL-depth profile to develop (usually at least one year), the site can be re-visited and the calibration surface (for which the exposure time is now well constrained) can be sampled and an OSL depth profile obtained. The model parameters μ and $\frac{\sigma \varphi_0}{\mu}$ are derived by fitting equation (1) to the calibration sample while using its known t ([Gliganic et al., 2019](#)). Once μ and $\frac{\sigma \varphi_0}{\mu}$ are derived the unknown rock surface exposure durations from the dating samples can – in principle – be obtained.

Because of the necessity to calibrate key model parameters for RSeD it follows that in order to obtain a correct rock surface exposure age the lithology-dependent parameters σ and μ must be the same in the dating and the calibration samples. Ideally, the lithology of the calibration sample matches that of the target sample as closely as possible also in terms of texture, grain size distribution and colour hue ([Meyer et al., 2018](#)). It has been shown that even mm-scale lithological changes between samples such as changes of the relative abundance of opaque minerals (e.g. biotite), or changes in the inclination of foliation planes can have a large impact on light tunnelling effects and thus OSL bleaching depths and the overall accuracy of RSeD ([Ou et al., 2018](#); [Meyer et al., 2018](#)).

The same is true for φ_0 , because any changes in the incoming photon flux will result in a change in the bleaching rate and thus influence OSL bleaching depths. The relative importance and influence of the model parameter φ_0 on OSL bleaching depths in relation to the other model parameters has never been quantified. We designed an experiment in order to investigate this influence empirically. The principal idea of the experiment is to expose rock samples of identical lithologies to natural sunlight at different aspects and inclinations for a time span long

enough, that bleaching profiles develop and differences in bleaching rates (φ_0) can be obtained. The experiment was conducted on granite and sandstone samples and the total insolation received by each sample surface was monitored with pyranometers for the entire duration of the experiment. The infrared-stimulated luminescence (IRSL) from feldspar and the optically stimulated luminescence (OSL) signal of quartz was examined from the granite and sandstone samples, respectively.

This experiment allowed us to (i) isolate φ_0 from the other parameters of the model of [Sohbati et al. \(2012a,b\)](#), (ii) evaluate the relative influence of φ_0 on the OSL bleaching depths, and (iii) investigate the relative importance of factors that impact φ_0 directly, such as aspect and inclination, total solar insolation and topographic shadowing effects. The data presented here thus contribute to our understanding of the complex interplay of processes responsible for propagation of OSL bleaching fronts into rock surfaces and thus foster the development of RSeD as a robust dating tool.

2. Materials and methods

2.1. Sample description

The natural bleaching experiments were performed on two types of lithology: a phaneritic fine-grained granite with a homogeneous distribution of light and dark minerals and a fine-grained and light-coloured sandstone (SOM 1). The granite is of unknown origin, but most probably comes from the Variszian Moldanubicum in eastern Austria. It is composed of quartz, potassium feldspar, plagioclase and biotite (SOM 1 a and c). The equigranular and fine-grained texture provides the granite samples a rather homogenous greyish to whitish colour hue. The fine-grained sandstone is from the Elbe sandstone mountains (Germany) and consists almost entirely of well sorted, sub-rounded quartz grains, with ancillary muscovite, rutile and tourmaline grains and lacks feldspar (SOM 1b and d). Most sandstone samples show macroscopically distinct brighter and darker bands (SOM 1 b) and thin section observations revealed that in the darker bands quartz grains are frequently coated by a thin film of hematite, while in the light bands hematite is almost non-existent (SOM 1 d). The differently coloured sandstone bands were deliberately targeted in this study and investigated separately.

2.2. Experimental setup

To make sure that no parts of the granite and sandstone samples were exposed to light prior to the start of the bleaching experiment, the outermost 5 cm of material of each sample were removed by sawing the samples to blocks 10 × 10 × 4 cm in dimension under red light conditions. Their sides were masked with two layers of lightproof adhesive tape to prevent light from entering the rock slabs laterally and thus to ensure that light only interacted with the frontal sample surfaces (SOM 2 c). These blocks were glued to a wooden mount, each holding one sandstone and one granite sample. The samples in their wooden mounts were then installed on the roof of the freestanding building of the University Innsbruck at 640 m above sea level (Bruno Sander Haus; N 47° 15' 51,36"/E 11° 23' 6,57"; SOM 2 b). The height of this building is 38 m and thus sufficient that the bleaching experiment could be conducted well above the skyline of the city of Innsbruck, unaffected by shadowing effects of any nearby buildings. Four samples were positioned on the outside walls of the staircase enclosure on top of the building to face approximately northwest (309°), northeast (39°), southeast (129°) and southwest (219°), respectively. One sandstone and one granite sample were placed horizontally (later also referred to as "Top"), i.e. with the rock face being oriented at 90° relative to the other samples and facing upward into the open sky (Supplementary online material SOM 2 b). All samples were kept on the roof for 108 days, from June 6th to October 25th 2019.

The amount of solar insolation reaching each sample was measured using pyranometers (Model SP-110 from Apogee Instruments) that were

facing the same direction as the samples (SOM 2 c). The SP-110 pyranometers record in the 360–1120 nm wavelength range and measure total (i.e. direct and indirect) insolation with highest sensitivity in the near infra-red due to respective filter characteristics (Apogee, 2020). Data acquisition was configured to obtain one insolation measurement per minute and record the hourly mean and standard deviation values calculated from this data.

Two types of calibrations were performed to ensure that the aspect-specific insolation values obtained via the SP-110 pyranometers are both accurate and precise. Firstly, Apogee Instruments specifies a factor for converting the readout signal (mV) to irradiance (W m^{-2}) of 5 W m^{-2} per mV. To be sure that this conversion factor is correct over the course of a day (and thus at different solar incident angles) we calibrated each sensor against a high precision global radiation sensor (Schenk-Sternpyranometer type 8102) that is permanently mounted on the rooftop of the Bruno Sander Haus as part of long-term meteorological observations. Corrections between 1 and 10% had to be applied to the sensors, depending on the time of the day (SOM 3). Secondly, the pyranometers were cross-calibrated against data from a high-precision global solar radiation sensor (Kipp & Zonen - type CM22) situated in a semi-automatic weather station at Innsbruck airport (~2.5 km from the Bruno-Sander-Haus) to ensure the overall accuracy of the insolation values (SOM 3). The reference instruments are operated within monitoring networks of the Austrian National Weather Services (ZAMG) and conform to highest international standards (Olefs et al., 2016).

2.3. Sample preparation, IRSL and OSL measurements and protocols

After a bleaching duration of 108 days, the sandstone and granite samples were transferred into the OSL laboratory for investigating their OSL and IRSL-depth curves, respectively. Under subdued red-light laboratory conditions the samples were cored through their full depth (4 cm) using a water-cooled diamond core drill and cores of 7.8 mm diameter were obtained. Multiple cores were obtained from each sample surface.

For the granite samples, three cores were drilled per aspect and the cores sliced at 0.85 mm increments using a Metkon Micracut 152 water-cooled low-speed saw and a sawblade of 0.25 mm thickness. The thickness of the resulting slices was between 0.4 and 0.8 mm. Intact rock slices obtained from these granite cores were mounted directly into aluminium cups for measurement of their IRSL signals. For the sandstone samples, at least two cores were obtained for each light- and dark-coloured sandstone band per sample (SOM 1 d). The sandstone was too fragile to obtain intact rock slices, but instead crumbled during sawing. The rock fragments for each slice were collected using filter paper, dried and gently crushed with an agate mortar to obtain the original grain size fraction. The grain size distribution obtained via this procedure was checked using ImageJ (Schindelin et al., 2012) on images obtained for each aliquot at the end of the OSL measurements inside the Risø TL/OSL reader with a built in sample camera. A grain size range of 50–250 μm was determined in this way for all aliquots. In order not to lose too much of the scarce sample material, we refrained from etching with HF. For the subsequent OSL measurements, the material retrieved from each sandstone slice was split into three aliquots (2 mm mask size).

All luminescence measurements were conducted in a Risø TL/OSL DA20 reader with a conventional coarse-grain-calibrated 90Sr/90Y beta source (Bøtter-Jensen et al., 2010). The granite aliquots were stimulated using IR LEDs (870 nm, $\sim 145 \text{ W/cm}^2$) and the IRSL signals measured via an Electron Tubes Ltd 9635 photomultiplier tube and a Corning 7–59 and Schott BG-39 filter combination (“blue filter pack”). A post-IR IRSL protocol was used for these measurements (Buylaert et al., 2012). This protocol involved preheating to 250 °C for 60 s, followed by an IR stimulation for 100 s at 50 °C (IR50) and a second IR stimulation for 100 s at 225 °C. The test dose was 79 Gy. For the IR50 and the pIR-IRSL225 signals, the initial 2 s minus a background from the last 10 s of the stimulation time were used for signal calculation. The same TL/OSL

reader was used for measuring the OSL of the quartz-rich extracts from the sandstone samples. Optical stimulation was performed with blue LEDs ($470 \pm 30 \text{ nm}$, $\sim 80 \text{ W/cm}^2$) at 125 °C for 55 s and the OSL detected through a 7.5 mm Hoya U304 filter. We measured the Lx/Tx values of quartz, which involved preheating to 220 °C for 30 s followed by IR stimulation for 50 s at 50 °C to reduce any eventual contributions from feldspar grains, followed by blue LED stimulation at 125 °C for 55 s (Banerjee et al., 2001; Murray and Wintle, 2000). The test dose here was 9.8 Gy. These post-IR blue OSL signals were background corrected by integrating the initial 1.6 s of the decay curve and subtraction the signal from the subsequent 4 s (early background subtraction; (Cunningham and Wallinga, 2010)).

2.4. RGB scans as proxy for rock colour

We investigated the variation of rock colour in all samples following Meyer et al. (2018). Therefore, we sawed the sample blocks in half and scanned the rock surfaces adjacent to each drill core trace. We used an Epson GT 10000 + scanner and scanned at a resolution of 1200 dpi. The colour profiles were extracted using the “plot profile” tool of the image processing tool ImageJ (Schindelin et al., 2012). In addition, for each core, an average RGB value was calculated from the sum of the three colour channels between 0 and 8 mm depth, which is approximately equivalent to depth interval in which all cores achieve saturation.

3. Results

3.1. Insolation data

The insolation data was recorded over a duration of 108 days (from June 11th to October 25th 2019). The values recorded by the horizontally oriented high precision global radiation sensor (Ph. Schenk, Type 8102) were nearly identical to those measured using the horizontally oriented calibrated Apogee SP 110 pyranometer, indicating that the Apogee SP 110 pyranometer based data are accurate (Fig. 1a–d). Hence, the total insolation measured by each pyranometer was integrated over the entire duration of the experiment and ranges from 209 to 590 Wm^{-2} , depending on aspect (Table 1).

Because the insolation data were determined on an hourly base, aspect-specific daily insolation curves can be generated and studied. The shape of the daily insolation curves from selected arbitrary sunny and cloudy days during summer and autumn are shown in Fig. 1. On a sunny summer day (10th of July; Fig. 1a), the NE sensor (facing 39°) records a maximum in the early morning. The SE (129°) sensor also receives most insolation in the morning, but with an insolation peak much broader compared to the NE sensor. The horizontal sensor (referred to as Top) attains the insolation peak around midday while the SW (219°) sensor receives its insolation maximum in the afternoon. The insolation peak of the NW (309°) facing sensor occurs between 4 and 6 p.m. and only during the summer months (Fig. 1a).

On cloudy days, this typical diurnal pattern of aspect-specific maximum insolation does not develop. The timing of the daily maxima of the individual sensors can vary significantly between cloudy days, because it is strongly controlled by the spatiotemporal cloud coverage pattern, which can be quite different for each cloudy day (Fig. 1c and d). For example, full cloud coverage occurred on the afternoon of July 11th (Fig. 1c) and the morning of July 12th (Fig. 1d), blocking direct sunlight. Under such conditions scattered (diffuse) solar radiation prevails, and all vertical facing sensors receive broadly similar amounts of radiation, while the horizontal sensor still measures higher intensities compared to the vertical sensors (Fig. 1c and d). Short clearing periods in the morning of the 11th of July and in the afternoon of the 12th July resulted in the development of weak insolation peaks of the respective (i.e. sun-facing) aspects. In October, when the sun's position is much lower compared to July, the SE, SW as well as the top sensors still record pronounced insolation maxima, while all other

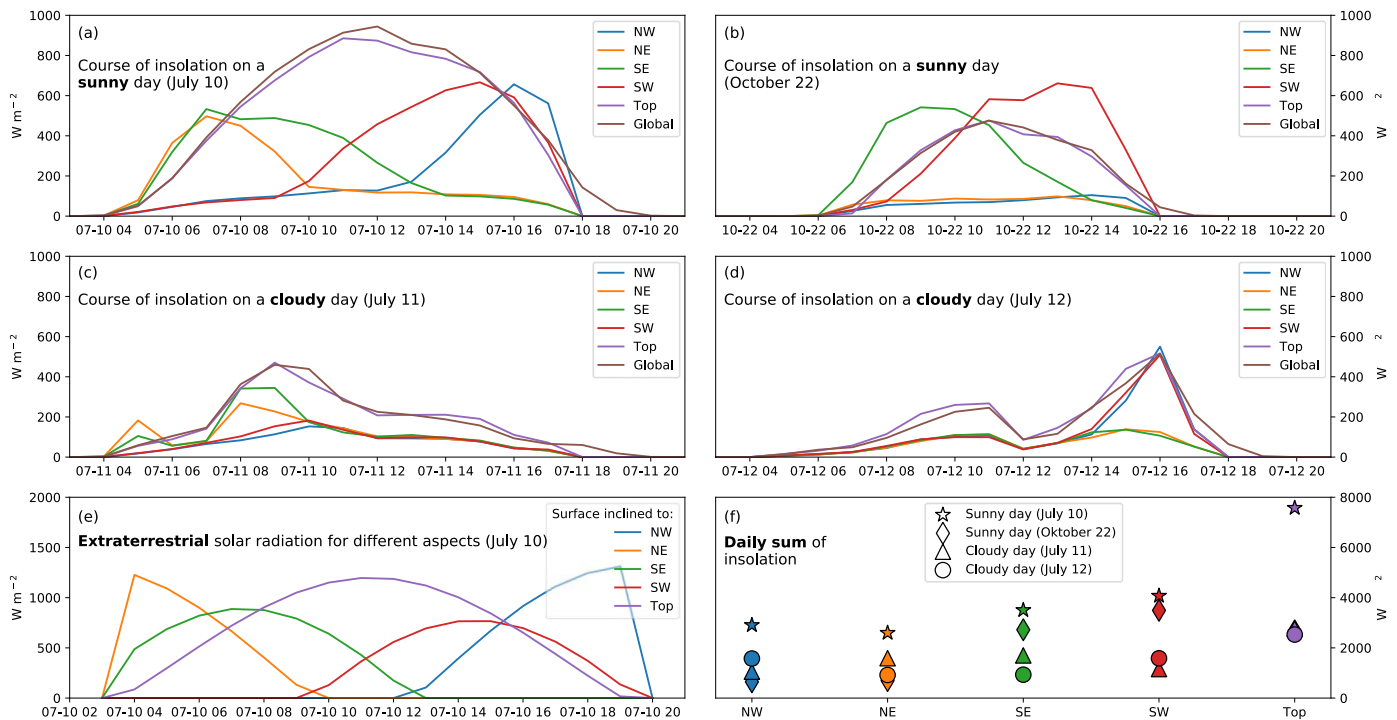


Fig. 1. Daily course of the measured insolation on two sunny ((a) and (b)) and two cloudy days ((c) and (d)). Subfigure (e) shows modelled, extraterrestrial (see Section: Results - insolation data) and aspect specific daily insolation curves. Comparison of those model results to the measured data confirms the validity of the measurements. The labels on the x-axis of subfigure (a), (b), (c), (d) and (e) indicate the month-date and hour of the day. Each plotted line presents one of the four compass directions (NW, NE, SE, SW), the Top sensor was placed horizontally (facing upwards). The global radiation was measured with a high-precision global solar radiation sensor and is used for reference and comparison with the Top sensor only. Subfigure (f) shows the sum of insolation at different aspects on sunny or cloudy days during summer and autumn.

Table 1

Total insolation measured in by each pyranometer all five orientations and integrated over the entire duration of the experiment and numbers of cores from each orientation and lithology that were used for constructing OSL and IRSL depth curves.

Aspect	Total insolation over the entire experiment [kWh m ⁻²]	Number of accepted cores		
		Sandstone dark	Sandstone light	Granite
NW (309°)	225	2	2	2
NE (39°)	209	2	0	3
SE (129°)	335	2	2	3
SW (219°)	414	2	2	3
Horizontal	590	2	3	3

insolation peaks are significantly less well developed (Fig. 1b). Interestingly, the absolute insolation values measured with the SE and SW sensors are similar in magnitude on a sunny day of October and July (Fig. 1a and b).

Furthermore, the total daily insolation on a sunny day is approximately three to five times that on a cloudy day, regardless of exposition of the sensor. The minimum insolation was measured on the northeast side on a cloudy day (38 w m⁻², Fig. 1d) and the highest insolation was measured on the horizontal sensor on a sunny day (305 W m⁻²; Fig. 1a).

3.2. OSL and IRSL depth profiles

From each sample surface and each aspect (i.e. granite, light and dark sandstone bands facing into NW, NE, SE and SW direction as well as up-ward (horizontal) into the open sky), three drill cores were obtained and sliced (Table 1). For some sandstone cores slicing suffered from a large depth error, and consequently these cores had to be rejected for

data analysis. The NE facing sandstone sample had no light band, hence only cores of the dark sandstone type could be sampled in this case (Table 1).

For all samples, the sensitivity-corrected natural signals (Lx/Tx) from each slice were normalized to the corresponding core's saturation level. The normalization factor was the weighted mean value of the deepest five Lx/Tx values, showing a saturation plateau, typically at depths >40–60 mm). A least-square best-fit algorithm based on Lehmann et al. (2019) was used to fit these luminescence-depth data via the first order model of Sohbati et al. (2012) (SOM 4 and 5). Fig. 2 shows these best-fit models that are based on at least one and up to three cores per sample surface. Furthermore, each individual core was also fitted with the same algorithm (SOM 4 and 5).

Both the light and dark sandstone bands in the sandstone samples that were exposed in a SE direction were bleached least (Fig. 2a and b). The OSL-depth profiles from the other aspects lie rather closely together and are bleached around 1 mm deeper than the OSL-depth profiles from the SE facing sample surface. Overall, the OSL-depth profiles from the light sandstone bands are bleached about 1 mm deeper compared to OSL-depth profiles from the dark sandstone bands. The slope of the bleaching profiles varies significantly between cores, regardless of aspect and sandstone colouring (Fig. 2a and b).

In the granite sample, the NW side was bleached least (~2.5 mm) and the SW side was bleached almost 2 mm deeper. All other directions lie between those two extremes and their bleaching depths are similar. In general, the IR50 signal bleaches around 1 mm deeper compared to the pIR225 signal (Fig. 2c and d).

3.3. RGB profiles

In Fig. 3, the RGB depth profiles that were obtained adjacent to each core are shown. For the granite cores, the RGB values fluctuate widely around a value of 380 ± 200. In contrast, the RGB profiles of the

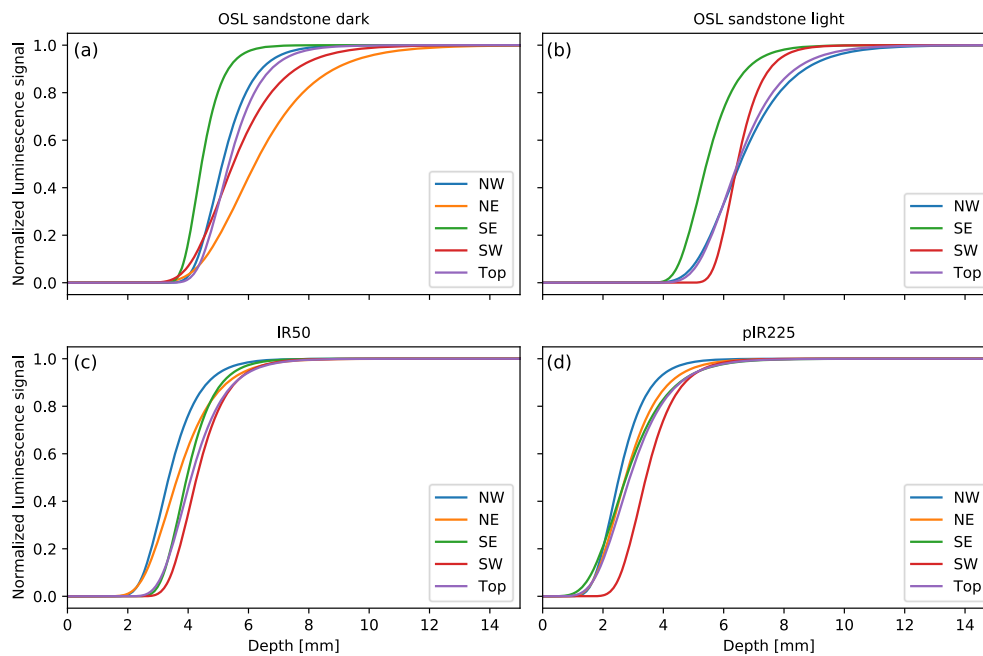


Fig. 2. Best fit models for the normalized OSL and IRSL depth profiles from the dark (a) and light (b) sandstone layers and the IR50 (c) and pIRIR225 (d) signals from granite. Note that for each aspect all cores were combined before the bleaching-with-depth model of [Sohbati et al. \(2012a,b\)](#) was applied. The individually fitted cores are shown in SOM 4 and 5, respectively.

sandstone cores are smooth with RGB values for the light and dark sandstone layers of ~ 700 and ~ 600 respectively ([Fig. 3](#)). Overall, all sandstone cores plot rather close to the maximum sum of RGB values of 800 underscoring that this particular sandstone type is very light.

3.4. Correlation of insolation versus bleaching depth and RGB values

[Fig. 4a](#), [c](#) and [e](#) show the total insolation that accumulated over the course of the experiment for each core from each aspect (labelled NW, NE, SE, SW and Top in [Fig. 4a](#)) on the x-axis. Each core is colour-coded according to its average RGB value (colour bar, right hand side), while the bleaching depth (i.e. depth at which the luminescence signal is at 50% of its maximum intensity) for each core is plotted on the y-axis. These figures allow examination of total insolation versus bleaching depth while considering the rock colour of each core (RGB values) at the same time. The same data are shown in a different way in [Fig. 4b](#), [d](#), and [f](#) in order to investigate the effect of rock colour (RGB values on the x axis) on bleaching depth (y axis) while still keeping track of the total insolation ranges via a colour coding scheme of the individual cores (compare legend in [Fig. 4b](#)).

The sandstone samples ([Fig. 4a](#) and [b](#)) show significant intra core variability in bleaching depth for each aspect (the bleaching depth varies between 1 and 2 mm for each aspect; [Fig. 4a](#)) and no clear relationship between bleaching depth and total insolation can be observed, neither in [Fig. 4a](#) nor [b](#). However, greater bleaching depths appear to be associated with higher RGB values (i.e. lighter rock colour; [Fig. 4a](#)). This becomes also obvious in [Fig. 4b](#), where a robust correlation between RGB value and bleaching depth ($R^2 = 0.55$) can be observed, while a correlation between total insolation (colour coding of cores) and bleaching depth is lacking.

In case of the granite samples the aspect-specific intra-core variability in bleaching depth is smaller than in sandstone samples (ranging from 0.5 to 1 mm only; [Fig. 4c](#) and [e](#)). This is true for both, the IR50 and pIR225 signals. Furthermore, the IR50 signal is bleached approximately 1 mm deeper than the pIRIR225 signal, corroborating many other studies showing that the pIRIR signal is generally more difficult to bleach than the IR50 signal ([Freiesleben, 2021](#)). There appears to be no correlation between bleaching depth and core specific RGB values in

[Fig. 4c](#) and [e](#). This is corroborated in [Fig. 4d](#) and [f](#), which show R^2 values 0.17 and 0.08 for the IR50 and pIR225 signals, respectively, which are statistically insignificant compared to the sandstone samples ([Fig. 4b](#)). However there appears to be some control of total insolation on bleaching depth. For both the IR50 and pIRIR225 signals, the vertically oriented samples (i.e., NW, NE, SW, and SE) clearly show that bleaching depth increases with total insolation. Interestingly, this relationship does not apply to the horizontally oriented top surface, which received the highest total insolation but was only bleached to a moderate depth (relative to the other surfaces).

3.5. Incidence angle of the sun and the sample surface

To test the effect of incidence angle of incoming light on the bleaching depth of the luminescence signal in our rock samples, the range of angles of incoming insolation needed to be assessed. With incidence angle we refer to the angle between the sample surface of our rock slabs and the sun, which can be anywhere between 90° (solar radiation hits the sample surface perpendicularly) and 0° (solar radiation runs parallel to rock surface). Following [Whiteman and Allwine \(1986\)](#), we calculated (i) the amount of extra-terrestrial insolation that hits each sample surface and (ii) the mean relative incidence angles between the sun and the sample surfaces. The extra-terrestrial insolation model was run over the entire duration of the bleaching experiment (i.e. 108 days) at a 5-min increment resolution ([Fuhrmann, 2021](#)), but does not consider any topographic shadowing effects.

Aspect-specific daily insolation curves were extracted from the model and are shown in [Fig. 1e](#). Comparing these extra-terrestrial (i.e. modelled) aspect-specific daily insolation curves ([Fig. 1e](#)) with the ones measured via our pyranometers ([Fig. 1a](#)) reveals that their shapes and the insolation patterns are broadly similar to each other, confirming the validity of the model. The only exceptions are the insolation curves from the NE (39°) and NW (309°) aspects, where the modelled insolation maxima are offset from the insolation maxima measured via our pyranometers; i.e. the NE pyranometer attains its maximum after the modelled value and vice versa for the NW aspect ([Fig. 1a](#) versus [e](#)). Because the city of Innsbruck, where the experiment was run, is surrounded by up to 2700 m high mountains, this effect is readily explained

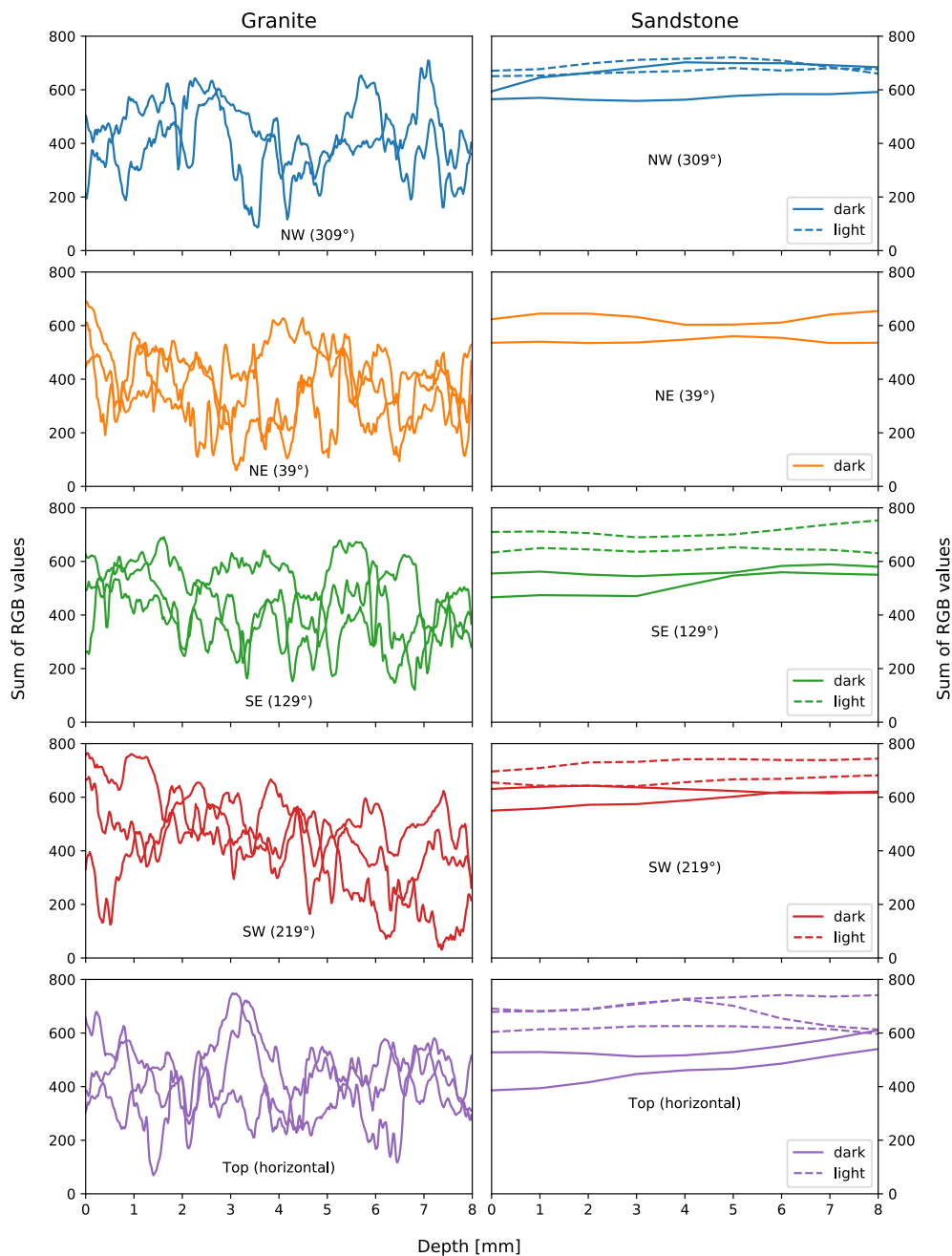


Fig. 3. RGB profiles of all cores from the granite (left column) and the sandstone samples (right column). The profiles start at the surface of the rock samples (0 mm) and end at 8 mm depth, which is for both rock types well within the saturation plateau auf the IRSL and OSL-depth curves. Note that on the y axis the sum of the 3 RGB channels (red, green and blue) are plotted.

by the local topography (SOM 6). Hence, the model was corrected for any local topographic shadowing effects in order to obtain an accurate probability density distribution of incident angles for each aspect. In Fig. 5a the resulting kernel density plots of the incident angles are shown together with the median value. The surfaces facing SW and NE show the highest median values (44.1° and 39.9°, respectively). The surface facing NW and SW experience the lowest median angles (19.3° and 25.3°, respectively). The horizontal surface that faces upwards into the open sky (receiving the highest total direct and indirect insolation), reveals a median incidence angle of 34.7°.

Fig. 5b shows the linear regression between the bleaching depth and the incidence angle. The R^2 values show significant correlation for the dark sandstone layers as well as for the IR50 and pIR225 signals (0.71, 0.45, 0.55 respectively).

4. Discussion

We have observed different bleaching depths for each orientation in all luminescence signals (OSL, IR50 and pIR225). There are various factors, in the rock samples themselves as well as environmental conditions (orientation, shielding effects caused by local topography, weather conditions), that potentially influence μ and $\overline{\sigma\phi_0}$ and therefore have an effect on the bleaching rate. Those factors are discussed individually below.

4.1. Variation of insolation with aspect

The amount of total insolation received by our pyranometers and thus rock sample surfaces is the sum of direct, indirect and diffuse

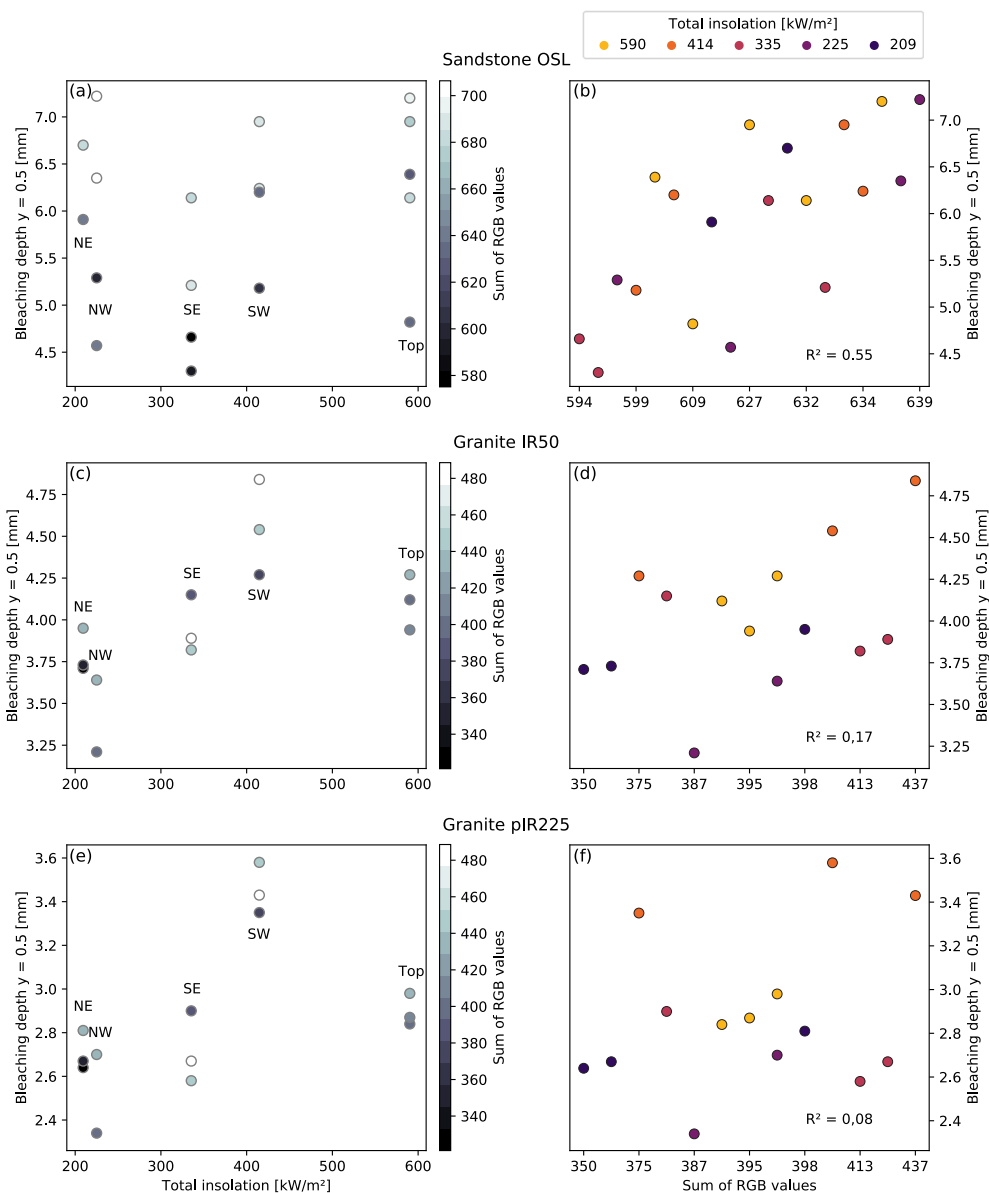


Fig. 4. Relation of bleaching depth, total insolation and RGB values for the granite and sandstone samples. (a, c and e): Insolation versus bleaching depth. The brightness of the rock (sum of RGB values) is indicated by brighter and darker colours. (b, d and f): RGB values versus bleaching depth. The amount of total insolation is shown by colour (see legend above Fig. 4b).

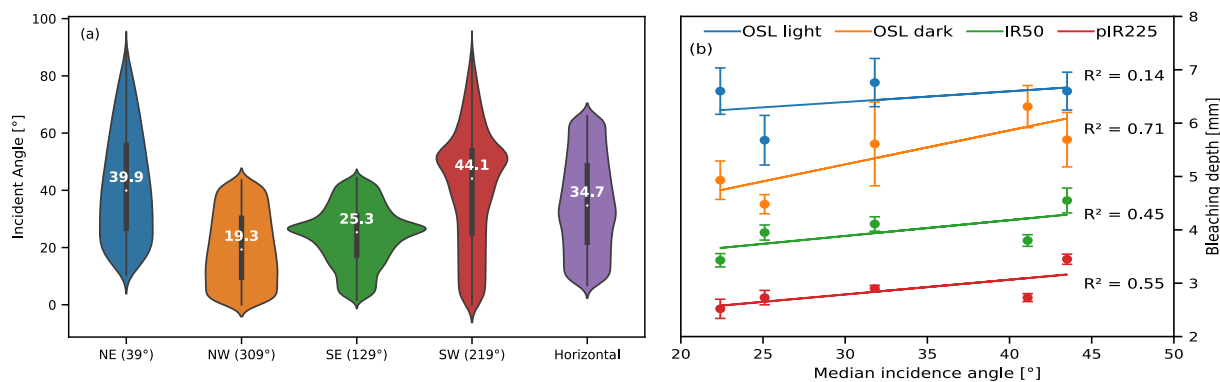


Fig. 5. (a) Smoothed probability density plots of the incident angles with the sun and the sample surfaces. The median incidence angle for the entire duration of the experiment (108 days) is shown for each orientation. (b) Linear regression of those median incidence angles with the bleaching depths for the different luminescence signals and the respective R^2 values.

insolation and varies at any given time with (i) the incidence angle between the sample surface and the sun, (ii) the local meteorological conditions, and (iii) shadowing, scattering and reflection effects due to the local topography. The incoming insolation is also strongly dependent on (iv) the total amount of time for which a given rock surface was exposed to the sum of the insolation components.

As far as direct solar radiation is concerned, the exposure angle changes on diurnal and seasonal timescales and strongly influences the solar insolation for each sample surface. Generally speaking, solar insolation is highest when the exposure angle is at 90° to the sample surface and solar insolation decreases with each degree of lowering of the exposure angle. Our experiment took place during summer to early autumn (6th June 2019 to 25th October 2019) and thus at a time when the sun followed a relatively steep apparent arc-like path in the sky, with a maximum solar altitude angle of 66° for Innsbruck on the 21st of June (summer solstice) and a minimum solar altitude angle of 30° at the end of the experiment (25th of October). Hence, during summer, the top sensor was in direct sunlight for most of the day and the exposure angle attained up to 66° . This is considered the main reason why the top sensor recorded the highest amount of total insolation during the course of this experiment (590 kW m^{-2} ; Table 1). The sensor facing SE on the other hand, is exposed to direct sunlight for many hours daily as well, but for the majority of the experiment the exposure angle was low (e.g. 33° on the 21th of June) because of the high apparent position of the sun during summer. The exposure angle for the SE sensor increased significantly towards autumn and was 66° on October 25th due to the much flatter apparent arc-like path of the sun at that time of the season. Because of such an increase in the exposure angle, on October 22nd the SE sensor received a higher maximum insolation compared to the top sensor (Fig. 1b). In our experiment the insolation was recorded during the summer season only rather than an entire year. Hence, the insolation record for the winter season is missing and incomplete for the spring and autumn months. This explains why the total amount of insolation determined for the SE-facing sensor and thus the SE facing rock panel was only 335 kW m^{-2} (Table 1).

The total insolation is also dependent on the local meteorological conditions. High cloud coverage blocks direct insolation and thus decreases the amount of total insolation, leaving diffuse (scattered) insolation as the only source of incoming solar radiation. On heavily overcast days, scattered light reaches the sensors rather uniformly from all directions and thus the sensor aspect does not play a major role anymore. This is documented in Fig. 1c and d, where heavy cloud coverage in the afternoon of July 11th (Fig. 1c) and morning of July 12th (Fig. 1d) diminished the insolation differences for all sensors. The exception is the upward facing top sensor, which received diffuse light but from a non-truncated hemispheric field of view, whereas all vertically-oriented sensors facing SE, SW, NE or NW, received light from a truncated hemisphere (i.e. the lower half of the hemispheric field of view is missing). Another consequence of a high cloud coverage is the shift of wavelengths towards infra-red. Compared to a sunny day, the spectrum on a cloudy day consists of a higher proportion of near infra-red light because of a lack of incoming direct sunlight due to shadowing from the clouds as well as back-scattered solar radiation from Earth's surface by the cloud cover.

The local topography is an additional major factor controlling the amount of aspect-specific direct insolation. This is especially relevant in an inner alpine setting such as the Inn valley, and thus for our experiment. The Inn valley is trending approximately NNE - SSW, and sunrise and sunset in Innsbruck on June 21st (longest day during experiment) occur at 53° and 307° azimuth, while on October 25th (shortest day during experiment) sunrise and sunset happen at 107° and 253° azimuth, respectively (Tiris, 2021; SOM 6). Particularly high azimuth values at sunsets during summer months are the reason for the high insolation values measured by the pyranometer oriented to the northwest – direct sunlight reaches the sensor right before sunset. These large differences of azimuth values between summer and autumn are caused by the

seasonally changing arc path of the sun as well as topographic effects of local mountain ranges. Topography of the neighboring mountains also cause a later sunrise and earlier sunset at certain times (see SOM 6).

In summary, we find that the aspect-specific total insolation is the result of a complex interplay between at least four major parameters: total exposure time, exposure angle, local meteorological conditions and topography.

4.2. Dependency of bleaching depth of OSL and IRSL profiles on rock opacity

Data shown in Fig. 4(b) confirms that bleaching depth significantly correlates with the colour of the rock ($R^2 = 0.55$) in the tested sandstone samples. This correlation suggests that the opacity of the rock exerts a more important control on the bleaching depth of our sandstone samples than insolation. Insofar these results are congruent with the model of Sohbaty et al. (2012a,b).

By contrast, the equigranular and fine-grained texture of the granite samples does not provide any predominantly lighter or darker areas. Consequently, no relationship between the rock colour and bleaching depth could be observed (compare Fig. 4d and f), with R^2 values of 0.17 and 0.08, respectively). These samples, thus, do not allow an assessment of the relationship between μ and bleaching depth, since μ is relatively consistent between cores.

4.3. Dependency of bleaching depth of OSL and IRSL profiles on insolation

The homogeneous texture and the small difference of colour hue in the granite compared to the sandstone allows an isolated view on the $\sigma\phi_0$ parameter and its impact on the formation of the bleaching front.

In the case of the vertically oriented NW, SE and SW granite samples, the bleaching depth shows some relationship with the total insolation. However, for the IR50 and pIR225 signals, the bleaching depth can be deeper in cores that were exposed to low total insolation than in samples that were exposed to higher total insolation. This is obvious, when comparing the bleaching depths of the cores from the SW and horizontally facing granite samples; even though the horizontal sensor was exposed to 50% more sunlight than the southwest sensor, the southwest facing sample is bleached deeper than the top sample (Fig. 4c and e). In addition, the sample that was oriented to the NE is bleached deeper than the sample that was oriented to the NW, even though it was exposed to less total insolation. These findings suggest that scattered or indirect light is not as effective in bleaching luminescence signals as direct sunlight is and that the bleaching rate in rock surfaces is strongly influenced by the angle at which sunlight strikes the rock surface.

4.4. Dependency of bleaching depth of OSL and IRSL profiles on incidence angle between the sun and the rock surface

In addition to the aspect-specific duration of insolation and the rock opacity (μ), a factor that has a high impact on the ϕ_0 parameter in the bleaching process is the incidence angle between the sun and the rock surface over the entire period of exposure to the sun. High incidence angles (close to 90°) are more efficient in bleaching than low incidence angles (close to 0°). In all the samples we investigated, the bleaching depth strongly correlates with the mean incidence angle during the experiment period (Fig. 5a and b). In summary, this means that for a given exposure duration, direct sunlight would bleach more deeply than indirect or scattered light. This implies that the azimuth and inclination at which bleaching is most effective will vary for every study location; for example, in the northern hemisphere, a south-facing rock surface that is inclined at an angle equal to the geographical latitude will be most efficient for bleaching. For dating purposes, these results indicate that calibration surfaces should have the same exposure aspect (including shadowing effects from local topography) as the target

unknown age dating surfaces, so that the bleaching profiles will be as similar as possible. A simple way of achieving this is to collect the target surface and return later to collect the sampling scar, which would have a precisely known exposure age and an identical lithology and exposure aspect as the target dating sample, thereby making it a best-case calibration sample.

4.5. Timescales

This experiment covers a period of 4 summer months (June–October). In summer months, the zenith angle of the sun is lower than in winter months. Because of this, the median incidence angles we observed for the vertically oriented samples during our experiment were generally lower than they would be if the experiment had lasted for an entire year. If the experiment had lasted an entire year, we would expect that the observed differences in incident angle dependency of the bleaching depth would be further aggravated. The horizontal samples would be exposed longer to sunlight coming from low angles, while the vertically oriented SE and SW samples would be illuminated from (more bleaching effective) high incidence angles for longer. This implies that there are seasonal cycles for the effectiveness of bleaching for a given rock surface (i.e., the bleaching effectiveness at a given site will change throughout the year according to season and orientation of the rock surface). From a RSeD application perspective, these results indicate that calibration surfaces should be exposed for at least a year and should be collected in approximately year increments, so that the calibration surface is not biased by any given season's insolation angle.

5. Conclusion

In our controlled exposure experiment the influence of φ_0 (photon flux at the rock surface) has been quantified empirically. Our data confirms that the bleaching depth is dependent on the light attenuation coefficient (μ) and, for vertically oriented samples, on the amount of total insolation. However, we also observed that bleaching rate in rock surfaces is strongly related to the incidence angle at which sunlight hits the rock surface. This hereto neglected variable may have a substantial impact on the accuracy of calibration in RSeD. In order to accurately calculate exposure ages of rock surfaces, $\overline{\sigma\varphi_0}$ and μ must be estimated correctly. For this, it is imperative to use the same lithology for the calibration sample as the sample itself. We strongly advise to find a piece of calibration sample that is of the same lithology and with identical rock properties (e.g. colour hue (μ)) as the dating sample. Our results suggest that for correct estimation of $\overline{\sigma\varphi_0}$, the spatial orientation (azimuth and inclination) of the calibration sample must match the dating sample as closely as possible. The approach of using the sampling scar as a calibration surface (Gliganic et al., 2019) is an optimal way of doing this – the calibration surface will have an identical azimuth and incidence angle as the target sample.

There will be seasonal cycles in the effectiveness of bleaching depending on the geographical location and the orientation of the rock sample; therefore, we suggest calibration samples should be left in year increments so that no season is preferred, though the more years a surface is exposed, the less the seasonal differences in bleaching will matter. When trying to date an unknown age surface, a calibration surface exposed for ~18 months (e.g., 2 winters and 1 summer such as Gliganic et al., 2019) is unlikely to yield an estimate of $\overline{\sigma\varphi_0}$ that would be appropriate for accurately modelling the target surface.

Declaration of competing interest

The authors declare that they have no known competing financial interests or personal relationships that could have appeared to influence the work reported in this paper.

Acknowledgements

Many thanks to Tanguy Racine and Benjamin Lehman for the fruitful discussions about data modelling and data analysis. We also thank the Department of Atmospheric and Cryospheric Sciences of the University of Innsbruck for providing the pyranometers. Intercomparison data were kindly provided by the Austrian National Weather Services (ZAMG). Finally we thank an anonymous reviewer for constructive feedback on the manuscript.

Appendix A. Supplementary data

Supplementary data to this article can be found online at <https://doi.org/10.1016/j.radmeas.2022.106732>.

References

- Apogee, 2020. SP-110 Pyranometer: owner's manual. Retrieved 15. Feb. 2020 from <https://www.apogeeinstruments.com/content/SP-110-manual.pdf>.
- Banerjee, D., Murray, A.S., Bøtter-Jensen, L., Lang, A., 2001. Equivalent dose estimation using a single aliquot of polymineral fine grains. *Radiat. Meas.* 33 (1), 73–94. [https://doi.org/10.1016/S1350-4487\(00\)00101-3](https://doi.org/10.1016/S1350-4487(00)00101-3).
- Bøtter-Jensen, L., Thomsen, K.J., Jain, M., 2010. Review of optically stimulated luminescence (OSL) instrumental developments for retrospective dosimetry. *Radiat. Meas.* 45 (3), 253–257. <https://doi.org/10.1016/j.radmeas.2009.11.030>.
- Brill, D., Klasen, N., Brückner, H., Jankaew, K., Scheffers, A., Kelletat, D., Scheffers, S., 2012. OSL dating of tsunami deposits from Phra Thong Island, Thailand. *Quat. Geochronol.* 10, 224–229. <https://doi.org/10.1016/j.quageo.2012.02.016>.
- Buylaert, J.-P., Jain, M., Murray, A.S., Thomsen, K.J., Thiel, C., Sohbati, R., 2012. A robust feldspar luminescence dating method for Middle and Late Pleistocene sediments. *Boreas* 41 (3), 435–451. <https://doi.org/10.1111/j.1502-3885.2012.00248.x>.
- Chapot, M.S., Sohbati, R., Murray, A.S., Pederson, J.L., Rittenour, T.M., 2012. Constraining the age of rock art by dating a rockfall event using sediment and rock-surface luminescence dating techniques. *Quat. Geochronol.* 13, 18–25. <https://doi.org/10.1016/j.quageo.2012.08.005>.
- Cunningham, A.C., Wallinga, J., 2010. Selection of integration time intervals for quartz OSL decay curves. *Quat. Geochronol.* 5 (6), 657–666. <https://doi.org/10.1016/j.quageo.2010.08.004>.
- Freiesleben, T., 2021. *Developing and Testing Models for Rock Surface Dating Using Optically Stimulated Luminescence*. Technical University of Denmark.
- Fuhrmann, S., 2021. Python Code to Calculate Incident Angle and Extra-terrestrial Solar Radiation on Inclined Surfaces. Github Repository. Retrieved 22.11.2021 from <https://github.com/SteFuh/incident-angle-of-sun-and-inclined-surface>.
- Gliganic, L.A., Meyer, M.C., May, J.-H., Aldenderfer, M.S., 2021. Direct dating of lithic surface artifacts using luminescence. *Sci. Adv.* 7 (23) <https://doi.org/10.1126/sciadv.abb3424>.
- Gliganic, L.A., Meyer, M.C., Sohbati, R., Jain, M., Barrett, S., 2019. OSL surface exposure dating of a lithic quarry in Tibet: laboratory validation and application. *Quat. Geochronol.* 49, 199–204. <https://doi.org/10.1016/j.quageo.2018.04.012>.
- Greilich, S., Glasmacher, U.A., Wagner, G.A., 2005. Optical dating of granitic surfaces. *Archaeometry* 47 (3), 645–665. <https://doi.org/10.1111/j.1475-4754.2005.00224.x>.
- Huntley, D.J., Godfrey-Smith, D.I., Thewalt, M.L.W., 1985. Optical dating of sediments. *Nature* 313, 105–107. <https://doi.org/10.1038/313105a0>.
- Jenkins, G.T.H., Duller, G.A.T., Roberts, H.M., Chiverrell, R.C., Glasser, N.F., 2018. A new approach for luminescence dating glaciofluvial deposits - high precision optical dating of cobbles. *Quat. Sci. Rev.* 192, 263–273. <https://doi.org/10.1016/j.quascirev.2018.05.036>.
- Laskaris, N., Liritzis, I., 2011. A new mathematical approximation of sunlight attenuation in rocks for surface luminescence dating. *J. Lumin.* 131 (9), 1874–1884. <https://doi.org/10.1016/j.jlumin.2011.04.052>.
- Lehmann, B., Herman, F., Valla, P.G., King, G.E., Biswas, R.H., . Evaluating post-glacial bedrock erosion and surface exposure duration by coupling in-situ OSL and ¹⁰Be dating. <https://doi.org/10.5194/esurf-2018-97>. *Earth Surf. Dynam. Discuss.* 1–38, 2019. <https://www.earth-surf-dynam-discuss.net/esurf-2018-97/>.
- Liritzis, I., 2011. Surface dating by luminescence: an overview. *Geochronometria* 38 (3), 292–302. <https://doi.org/10.2478/s13386-011-0032-7>.
- Liu, J., Cui, F., Murray, A.S., Sohbati, R., Jain, M., Gao, H., Li, W., Li, C., Li, P., Zhou, T., Chen, J., 2019. Resetting of the luminescence signal in modern riverbed cobbles along the course of the Shiyang River, China. *Quat. Geochronol.* 49, 184–190. <https://doi.org/10.1016/j.quageo.2018.04.004>.
- Meyer, M.C., Gliganic, L.A., Jain, M., Sohbati, R., Schmidmair, D., 2018. Lithological controls on light penetration into rock surfaces – implications for OSL and IRSL surface exposure dating. *Radiat. Meas.* 120, 298–304. <https://doi.org/10.1016/j.radmeas.2018.03.004>.
- Murray, A.S., Wintle, A.G., 2000. Luminescence dating of quartz using an improved single-aliquot regenerative-dose protocol. *Radiat. Meas.* 32 (1), 57–73. [https://doi.org/10.1016/S1350-4487\(99\)00253-X](https://doi.org/10.1016/S1350-4487(99)00253-X). <https://www.sciencedirect.com/science/article/pii/S135044879900253X>.

- Olefs, M., Baumgartner, D.J., Obleitner, F., Bichler, C., Foelsche, U., Pietsch, H., Rieder, H.E., Weihs, P., Geyer, F., Haiden, T., Schöner, W., 2016. The Austrian radiation monitoring network ARAD – best practice and added value. *Atmos. Meas. Tech.* 9 (4), 1513–1531. <https://doi.org/10.5194/amt-9-1513-2016>.
- Ou, X., Roberts, H., Duller, G., Gunn, M., Perkins, W., 2018. Attenuation of light in different rock types and implications for rock surface luminescence dating. *Radiat. Meas.* 120, 305–311. <https://doi.org/10.1016/j.radmeas.2018.06.027>.
- Polikreti, K., 2007. Detection of ancient marble forgery: techniques and limitations. *Archaeometry* 49 (4), 603–619. <https://doi.org/10.1111/j.1475-4754.2007.00325.x>.
- Polikreti, K., Michael, C.T., Maniatis, Y., 2003. Thermoluminescence characteristics of marble and dating of freshly excavated marble objects. *Radiat. Meas.* 37 (1), 87–94. [https://doi.org/10.1016/s1350-4487\(02\)00088-4](https://doi.org/10.1016/s1350-4487(02)00088-4). <https://www.sciencedirect.com/science/article/pii/S1350448702000884>.
- Rhodes, E.J., 2011. Optically stimulated luminescence dating of sediments over the past 200,000 years. *Annu. Rev. Earth Planet Sci.* 39, 461–488. <https://doi.org/10.1146/annurev-earth-040610-133425>.
- Schindelin, J., Arganda-Carreras, I., Frise, E., Kaynig, V., Longair, M., Pietzsch, T., Preibisch, S., Rueden, C., Saalfeld, S., Schmid, B., Tinevez, J.-Y., White, D.J., Hartenstein, V., Eliceiri, K., Tomancak, P., Cardona, A., 2012. Fiji: an open-source platform for biological-image analysis. *Nat. Methods* 9 (7), 676–682. <https://doi.org/10.1038/nmeth.2019>.
- Simkins, L.M., Simms, A.R., DeWitt, R., 2013. Relative sea-level history of Marguerite Bay, Antarctic Peninsula derived from optically stimulated luminescence-dated beach cobbles PANGAEA. <https://doi.org/10.1594/PANGAEA.818537>.
- Simms, A.R., DeWitt, R., Kouremenos, P., Drewry, A.M., 2011. A new approach to reconstructing sea levels in Antarctica using optically stimulated luminescence of cobble surfaces. *Quat. Geochronol.* 6 (1), 50–60. <https://doi.org/10.1016/j.quageo.2010.06.004>.
- Sohbati, R., Murray, A., Jain, M., Buylaert, J.-P., Thomsen, K., 2011. Investigating the resetting of OSL signals in rock surfaces. *Geochronometria* 38 (3), 249–258. <https://doi.org/10.2478/s13386-011-0029-2>.
- Sohbati, R., Murray, A.S., Buylaert, J.-P., Almeida, N.A.C., Cunha, P.P., 2012a. Optically stimulated luminescence (OSL) dating of quartzite cobbles from the Tapada do Montinho archaeological site (east-central Portugal). *Boreas* 41 (3), 452–462. <https://doi.org/10.1111/j.1502-3885.2012.00249.x>.
- Sohbati, R., Murray, A.S., Chapot, M.S., Jain, M., Pederson, J., 2012b. Optically stimulated luminescence (OSL) as a chronometer for surface exposure dating. *J. Geophys. Res. Solid Earth* 117 (B09202), 1–7. <https://doi.org/10.1029/2012jb009383>.
- Tiris, 2021. Sonnengangberechnung Tirol. Retrieved 12. 04. 2021 from. <http://tiris.tirol.gv.at/web/index.cfm>.
- Whiteman, C.D., Allwine, K.J., 1986. Extraterrestrial solar radiation on inclined surfaces. *Environ. Software* 1 (3), 164–169. [https://doi.org/10.1016/0266-9838\(86\)90020-1](https://doi.org/10.1016/0266-9838(86)90020-1).